

NUMERICAL DESCRIPTION OF MOVING SINGLE BUBBLE SONOLUMINESCENCE STATE IN SULFURIC ACID

Ludmila M. Rechiman^a, Damián H. Dellavale^a and Fabián J. Bonetto^a

^a*Laboratorio de Cavitación y Biotecnología. Instituto Balseiro-UNCu-CNEA-CONICET. Centro Atómico Bariloche CP(R8402AGP), Río Negro, Argentina.*

Keywords: Bubble Dynamics, SBSL, Non-Linear systems, History force.

Abstract. In the present paper a numerical model which describes the radial dynamics of a strongly forced periodic oscillating bubble coupled with the translational motion in a highly viscous liquid like sulfuric acid solutions was developed. All hydrodynamics forces acting on the bubble were considered in the model. A novel method to account for the History force on bubbles with variable radius is presented. As a result the m-SBSL state characterized by pseudo-orbits made by the translating bubble near the pressure antinode of a spherical acoustic field is described. The dependence of the bubble mean levitation position with the amplitude of the driving pressure was numerically simulated and analyzed. The numerical model at low forcing pressures was compared with an analytical solution. The agreement between them is good in the range of driving frequencies typically used in SBSL. It is also shown that the proposed algorithm successfully reproduces the path instability of previous reported Argon bubbles in Ethylene Glycol.

1 INTRODUCTION

The isolation of a single sonoluminescent bubble first achieved by [Gaitan et al. \(1992\)](#) (SBSL) encouraged the study of a transient cavity trapped in an acoustic field in a highly controlled manner. SBSL is a remarkable example of energy focusing phenomena using the fact that bubbles can respond to pressure forces in a non-linear way under very specific conditions. As the main goal is to achieve higher temperatures inside the bubble, liquids with low vapor pressure, as sulfuric acid solutions, have been used by many researchers: [Flannigan and Suslick \(2005\)](#), [Hopkins et al. \(2005\)](#), [Urteaga et al. \(2007\)](#), [Urteaga and Bonetto \(2008\)](#), [Dellavale et al. \(2012\)](#). The presence of vapor during main collapse does not favor the goal to achieve higher energy concentrations and higher temperatures because water dissociation effects absorb part of the mechanical energy available, [Puente and Bonetto \(2005\)](#). The high viscosity of this liquid prevents the pinch-off of the bubble during main collapse due to Rayleigh-Taylor shape instability as the acoustic pressure is increased. The use of this highly viscous liquid revealed a curious effect in which the bubble, periodically excited, moves through the fluid describing pseudo-orbits. This new state was first reported by [Didenko et al. \(2000\)](#) and it is known as moving-SBSL (m-SBSL). See Fig.(1). [Toegel et al. \(2006\)](#) shows that this “spatial instability” is due to the action of the history force on the bubble. His calculations and comparisons with experiments were made in another viscous liquid: Ethylene Glycol. The numerical model of [Toegel et al. \(2006\)](#) was based on the analytical expression developed by [Magnaudet and Legendre \(1998\)](#) of the hydrodynamic force experienced by a spherical bubble which has a variable radius. Further numerical investigations of the m-SBSL state were made by [Sadighi-Bonabi et al. \(2009\)](#), [Galavani et al. \(2010\)](#), [Mirheydari et al. \(2011\)](#) and [Sadighi-Bonabi et al. \(2011\)](#). However, all these calculations are based on the same numerical scheme of [Toegel et al. \(2006\)](#) and were made in an organic viscous liquid named N-methylformamide.

In this work we propose a different scheme to solve the coupled radial and translational dynamics of a strongly collapsing bubble based on the “window method” to compute the history force. In addition, we present a comprehensive analysis of all the forces acting on a translating Argon bubble in a 85%w/w sulfuric acid solution (SA85) in the parameter range in which the bubble is sonoluminescent.

The paper is organized as follows: in Sec.(2) we describe the coupling between the radial dynamics and the translational motion. Details of the numerical scheme developed to calculate the history force are also given in Sec.(2). In Sec.(3) we show the evolution of all the hydrodynamics forces acting on an Argon bubble in SA85 in the time scale of a radial period. In Sec.(4) we show the hydrodynamic forces over a larger time scale in which the spatial movement of the bubble in SA85 is visible. In Sec.(5) we theoretically analyze the positional instability as a function of the driving pressure amplitude. In Sec.(6) we compared the solution of the proposed model for the translational motion of a bubble subjected to very small radial oscillations with an analytical solution for bubbles with fixed radius translating in an accelerating liquid. In Sec.(7) we show the pseudo-orbits described by an Argon bubble in Ethylene Glycol in comparison with the state-of-art of m-SBSL simulations and finally in Sec.(8) we summarize our conclusions.

2 THE MODEL

2.1 Radial Dynamics

To describe the radial dynamics of the bubble we used the Keller-Miksis form of Rayleigh-Plesset Equation (RPE) [Keller \(1980\)](#). This model considered the radiation dumping effect

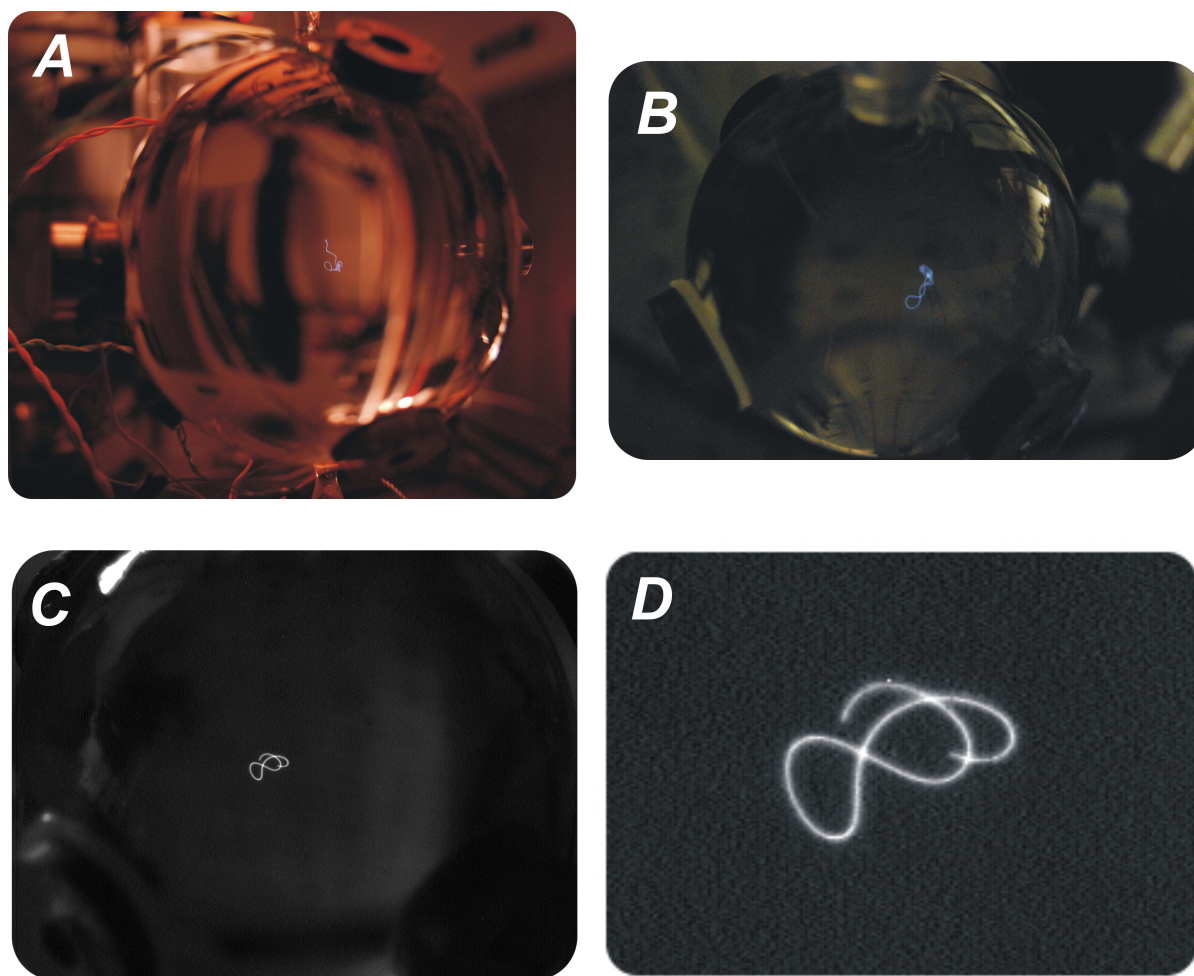


Figure 1: Experimental observations of m-SBSL of a bubble in SA85. The experiments were carried out in the Laboratorio de Cavitación y Biotecnología of Instituto Balseiro at Centro Atómico Bariloche. (A) Photograph of the m-SBSL state in the experimental setup of [Urteaga and Bonetto \(2008\)](#). The spherical resonator has an external diameter of 89 mm and was made of borosilicate glass. Attached to the very thin walls of approximately $250\mu\text{m}$ are glued the piezoceramic transducer drivers. (B) Photograph of the m-SBSL state of an Argon bubble in the experimental setup of [Dellavale \(2012\)](#). The spherical resonator was made of quartz and has an external diameter of 60 mm. The flask walls have 1 mm thickness. The photograph was taken by a Nikon D50 camera with a totally open diaphragm and the integration time was 1 second. The concentration of Argon gas dissolved in the liquid was 16 mbar. (C) Photograph of the m-SBSL state of an Argon bubble in the experimental setup of [Dellavale \(2012\)](#) using Hitachi KPF120 monochrome CCD camera with a totally open diaphragm. The integration time was 350 milliseconds. The size of the orbit was $dr \simeq 3\text{mm}$ located in a mean radial position shifted from the center of the flask $r < 4\text{mm}$. The concentration of Argon gas dissolved in the liquid was 16 mbar. (D) A closer look of the pseudo-orbit described by the translating Argon bubble of case (C). The pictures were taken by Dr. Damián Dellavale.

through the time derivative of gas pressure, and liquid compressibility is taken into account up to first order. We neglect the presence of vapor inside the bubble, provided the low vapor pressure of SA85 ($p_v = 2.45\text{ Pa}$). Then, condensation and evaporation effects inside the bubble are not included. The Keller-Miksis form of RPE can be written as follows:

$$\left(1 - \frac{\dot{R}(t)}{c_l}\right)R(t)\ddot{R}(t) + \frac{3}{2}\dot{R}^2(t)\left(1 - \frac{\dot{R}(t)}{3c_l}\right) = \frac{1}{\rho_l}\left(1 + \frac{\dot{R}(t)}{c_l}\right)(p_g(R(t)) - p(r, t)) + \frac{R(t)\dot{p}_g(R(t))}{\rho_l c_l} - \frac{4\nu_l\dot{R}(t)}{R(t)} - \frac{2\sigma}{\rho_l R(t)} \quad (1)$$

In Eq.(1), $R(t)$ is the radius of the bubble, $\dot{R}(t)$ is the radial velocity of the bubble interface, $\ddot{R}(t)$ is the radial acceleration of the bubble interface, ρ_l is the liquid density, c_l is the speed of sound in the liquid, σ is the surface tension, ν_l is the kinematic viscosity of the liquid, $p_g(R(t))$ is the pressure of the gas contents inside the bubble and $p(r, t)$ denotes the driving pressure field.

The radial dynamics of the bubble is fully dependent on the model used to compute the heat exchange between the gas and the liquid across the interface. The model must represent the isothermal evolution of the gas during the rarefaction phase of the acoustic cycle (expansion of the bubble) and the adiabatic evolution in the final stage of main collapse. In this work we assume that the pressure profile of the gas $p_g(R(t))$ is uniform inside the bubble and that the gas follows a polytropic evolution:

$$p_g(R(t)) = \left(p_0 + \frac{2\sigma}{R_0} \right) \left[\frac{R_0^3 - h^3}{R^3(t) - h^3} \right]^{\gamma(R, \dot{R}, T)} \quad (2)$$

In Eq.(2), $\gamma(R, \dot{R}, T_b)$ is the variable polytropic coefficient given by Hilgenfeldt et al. (1999):

$$\gamma(R, \dot{R}, T_b) = 1 + (\Gamma - 1) \exp \left[- \frac{A}{Pe(t)^B} \right], \quad (3)$$

$$Pe(t) = \frac{R(t)|\dot{R}(t)|}{\chi_g(R(t))}.$$

In Eq.(3), Pe is the Péclet number, Γ is the adiabatic coefficient of the gas, $\chi_g(t) = \frac{k_g}{\rho_g(R(t))cp_g}$ denotes the thermal diffusivity of the gas, k_g is the thermal conductivity, ρ_g is the gas density, cp_g is the specific heat at constant pressure and the constant parameters are: $A = 5.8$ and $B = 0.6$.

The time derivative of gas pressure is:

$$\dot{p}_g(t) = -\gamma(R, \dot{R}, T_b) \frac{3R^2(t)\dot{R}(t)}{R^3(t) - h^3} p_g(t) \quad (4)$$

The temperature profile of the gas T_b is also considered uniform inside the bubble. The time variation of the gas temperature is obtained from the van der Waals process equation plus a diffusive heat loss term which has influence during the afterbounce phase of the oscillations Hilgenfeldt et al. (1999),

$$\dot{T}_b = -[\gamma(R, \dot{R}, T_b) - 1] \frac{3R^2(t)\dot{R}(t)}{R^3(t) - h^3} T_b(t) - \chi_g \frac{T_b(t) - T_0}{R^2(t)} \quad (5)$$

In Eq.(5), T_0 is the ambient temperature and h is the Van der Waals hard core radius of the gas. The bubble is located within a spatial-time varying pressure field $p(r, t)$. Assuming a spherical geometry, the spatial distribution of the pressure field within the resonator is given by the zero-order spherical Bessel function $J_0(r) = \frac{\sin(k_0 r)}{k_0 r}$ Akhatov et al. (1997), then the pressure field forcing the bubble is:

$$p(r, t) = p_0 - \frac{\sin(k_0 r)}{k_0 r} p_a^0 \sin(2\pi f_0 t) \quad (6)$$

In Eq.(6), p_0 is the uniform ambient pressure, $k_0 = \frac{2\pi f_0}{c_l}$ is the wave number of the fundamental mode, p_a^0 is the amplitude of the acoustic pressure at the center of the volume (resonator), f_0 is the fundamental driving frequency ($T = \frac{1}{f_0}$) and $r = \sqrt{x^2 + y^2 + z^2}$ is the distance from the origin of coordinates. The amplitude of the pressure applied on the bubble at position r_b is $p_a^b = \frac{\sin(k_0 r_b)}{k_0 r_b} p_a^0$. Although, the acoustic pressure on the bubble at position r_b (p_a^b) is reported in most sonoluminescent works, in this paper we will report the pressure at the resonator center p_a^0 , which is the control parameter.

The liquid velocity can be analytically calculated by linearizing Navier-Stokes equation and neglecting viscous stress and volume forces, [Toegel et al. \(2006\)](#):

$$\vec{u}_l(r, t) = -\frac{1}{\rho_l} \int_0^t \nabla p(r, \tau) d\tau \tag{7}$$

2.2 Translational Dynamics

In this section, the translational dynamics of the bubble is taken into account together with the highly nonlinear radial oscillations forced by the driving acoustic pressure. [Magnaudet and Legendre \(1998\)](#) indicated that this problem is characterized by two dimensionless numbers: the translational Reynolds $Re_t = \frac{R(t)|\vec{U}(r,t)|}{\nu_l}$ where $\vec{U}(r, t) = \vec{V}_b - \vec{u}_l(r, t)$ is the relative velocity between the bubble translational velocity and the liquid velocity, and the radial Reynolds $Re_r = \frac{R(t)|\dot{R}(t)|}{\nu_l}$. Particularly, the history force is acting on the bubble when the bubble size is maximum and the translation is at low Re_t ($Re_t < 1$). The translational motion of the bubble has been calculated taking into account all the forces acting on it. The force balance on the bubble is of the form:

$$\begin{aligned} \vec{F}_b &= -\frac{4}{3}\pi R^3(t)\nabla p(r, t) - \frac{2}{3}\pi\rho_l \frac{d(R^3(t)\vec{U}(r, t))}{dt} - 6\pi\rho_l\nu_l R(t)\vec{U}(r, t) - \frac{4}{3}\pi\rho_l R^3(t)\vec{g} \quad \text{if } Re_t \text{ or } Re_r \gg 1 \\ \vec{F}_b &= -\frac{4}{3}\pi R^3(t)\nabla p(r, t) - \frac{2}{3}\pi\rho_l \frac{d(R^3(t)\vec{U}(r, t))}{dt} - 6\pi\rho_l\nu_l R(t)\vec{U}(r, t) - \frac{4}{3}\pi\rho_l R^3(t)\vec{g} - \\ &\quad - 8\pi\rho_l\nu_l \int_{-\infty}^t \exp\left[9\nu_l \int_{\tau}^t \frac{1}{R^2(s)} ds\right] \operatorname{erfc}\left[\sqrt{9\nu_l \int_{\tau}^t \frac{1}{R^2(s)} ds}\right] \frac{d}{d\tau}(R(\tau)\vec{U}(r, \tau)) d\tau \quad \text{if } Re_t \text{ and } Re_r \ll 1 \end{aligned} \tag{8 a,b}$$

In Eq.(8 a,b), the first term is the Bjerknes force, which results from the interaction between the gradient of the pressure field and the bubble volume oscillations. The second term is the added mass force, which is the result of an accelerating or decelerating body that displaces some volume of the surrounding fluid as it moves. The third term is the steady drag, which increases in a linear form with the relative velocity because of the low characteristic translational Re_t number of the present problem and the fourth term is the buoyant force. For slow radial and translating dynamics, the history force must also be taken into account (Eq.(8b)). It should be emphasized that the history force is non-local in time. The integral term in Eq.(8b) shows that the value of the history force depends on the past evolution of the bubble dynamics. A further treatment of this force will be given in Sec.(2.3).

The steady drag force of the present model takes into consideration a dirty bubble [Batchelor \(1967\)](#), given that bubbles of less than $100\mu m$ are more likely to suffer surfactant deposition on its surface [Leighton \(1994\)](#).

According to [Magnaudet and Legendre \(1998\)](#) there exist critical values for the Reynolds numbers, in particular $Re_t^c = 0.5$ and $Re_r^c = 7.0$ for the activation or deactivation of the history

force. The smooth transition between both dynamics was first made by [Toegel et al. \(2006\)](#) by introducing switches of the form :

$$\begin{aligned}\theta_r(t) &= \frac{1}{1 + \left[\frac{Re_r(t)}{Re_r^c} \right]^4} \\ \theta_t(t) &= \frac{1}{1 + \left[\frac{Re_t(t)}{Re_t^c} \right]^4}.\end{aligned}\tag{9}$$

Finally Eq.(8 a,b) are rewritten as follows:

$$\begin{aligned}\vec{F}_b &= -\frac{4}{3}\pi R^3(t)\nabla p(r,t) - \frac{2}{3}\pi\rho_l \frac{d(R^3(t)\vec{U}(r,t))}{dt} - 6\pi\rho_l\nu_l R(t)\vec{U}(r,t) - \frac{4}{3}\pi\rho_l R^3(t)\vec{g} - \\ &- \theta_t(t)\theta_r(t)8\pi\rho_l\nu_l \int_{-\infty}^t \exp\left[9\nu_l \int_{\tau}^t \frac{1}{R^2(s)} ds\right] \operatorname{erfc}\left[\sqrt{9\nu_l \int_{\tau}^t \frac{1}{R^2(s)} ds}\right] \frac{d}{d\tau}(R(\tau)\vec{U}(r,\tau))d\tau\end{aligned}\tag{10}$$

The system of Eq.(1),(5) and (10) is non-autonomous and was solved by double-stepping adaptive step-size Runge-Kutta algorithm [Press et al. \(1992\)](#). It is important to point out that in the present work we do not neglect the inertia of the bubble, though $\vec{F}_b = m_b\vec{a}_b \neq 0$ where m_b is the mass of the bubble and \vec{a}_b is the translational acceleration of the bubble.

2.3 HISTORY FORCE

The history force is related to the unsteady viscous flow developed behind a moving body. Many expressions for the history force on bubbles with constant radius in an unsteady flow at finite Reynolds number have been formulated: [Yang and Leal \(1991\)](#), [Mei et al. \(1994\)](#).

Namely, [Magnaudet and Legendre \(1998\)](#) developed an analytical expression for the history force acting on a translating bubble in the zero-Reynolds(translational) regime but with variable radius.

Based on this analytical formulation, it can be seen that Eq.(10) is an integrodifferential equation for the bubble position. In Eq.(10) the most time-consuming contribution is associated with computation of the history force integral. The calculation of the history force involves large storage efforts and requires the integration over the entire lifetime of the bubble. For example, the simulation of 10000 radial cycles, which involves approximately 1000 integration steps each, requires of 1.2 Gb memory for storing the 15 variables (double-precision floating point: 8 bytes) to solve the history force in Eq.(10).

In the present work we solve Eq.(10) with an approach different from the one implemented by [Toegel et al. \(2006\)](#). As a first step we approximate the kernel of the integral of the history force model in Eq.(10) by the solution proposed by [Ren and MacKenzie \(2007\)](#):

$$K(t, \tau) = \exp(H)\operatorname{erfc}(\sqrt{H}) \simeq \frac{a}{(a-1)\sqrt{\pi H} + \sqrt{\pi H + a^2}}\tag{11}$$

In Eq.(11), the constant is $a = 2.9110$. This value for a is selected as the one that minimizes the relative error, and H denotes the integrals $H = 9\nu_l \int_{\tau}^t \frac{1}{R^2(s)} ds$. Fig.(2) shows the value of the kernel used in the model of [Magnaudet and Legendre \(1998\)](#) and the approximation using the form of [Ren and MacKenzie \(2007\)](#). For a wide range of H values, the relative error is less than 0.3%. By using this approximation we avoid overflow problems in the case of large H

arguments. In the upper panel of Fig.(2), the type of convergence of the kernel when $H \rightarrow \infty$ then $K(t, \tau) \rightarrow 0$ can be seen. This implies that the contributions to the force at the present time from very previous times are less important than the contributions from the immediate past time.

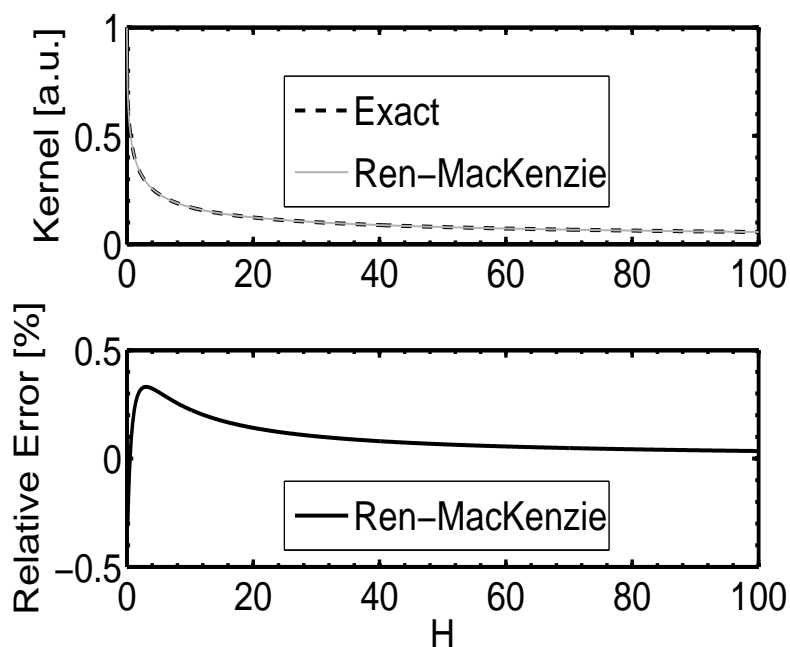


Figure 2: Solution of the history force kernel model and the approximation proposed by [Ren and MacKenzie \(2007\)](#).

One possible method to solve the Eq.(10) is to evaluate the integral of the history force at each time integration step of the coupled ODE ¹ system. To make this possible, we stored 15 variables involved in the argument of the history integral: t , $R(t)$, $\dot{R}(t)$, $u_l^x(r, t)$, $u_l^y(r, t)$, $u_l^z(r, t)$, $\dot{u}_l^x(r, t)$, $\dot{u}_l^y(r, t)$, $\dot{u}_l^z(r, t)$, $\dot{x}_b(t)$, $\dot{y}_b(t)$, $\dot{z}_b(t)$, $\ddot{x}_b(t)$, $\ddot{y}_b(t)$ and $\ddot{z}_b(t)$. Here, the subscript “ l ” denotes the liquid, while “ b ” indicate bubble. Strictly speaking, we should store all the bubble evolution from the very beginning of the simulation. This has the drawback of the time required to evaluate the integral at each time step. Also the model of the history force is valid a finite time backwards as it was indicated by [Magnaudet and Legendre \(1998\)](#).

[Dorgan and Loth \(2007\)](#) and [van Hinsberg et al. \(2011\)](#) implemented a truncated integration interval to calculate the Basset force (analogous to history force but for particles with fix radius) which requires storage and integration over a much shorter period of a particle’s history.

So the next question to answer must reconcile the computing time of the history force, the validity of the model to reproduce the physical effect and the validity of the method used to solve the history force integral: How long backwards do we have to consider the dynamics to calculate the history force?.

[Dorgan and Loth \(2007\)](#) indicated in their work that the “window model” is valid if the term $\frac{d(R\vec{U})}{dt}$ varies slowly, then:

$$\int_{t-t_{win}}^t K_{win}(t, \tau) d\tau \simeq \int_{-\infty}^t K(t, \tau) d\tau \quad (12)$$

¹ODE: ordinary differential equation

$$K_{win}(t, \tau) = \begin{cases} K(t, \tau) & t - t_{win} < \tau < t \\ 0 & \tau < t - t_{win} \end{cases} \quad (13)$$

Following this criteria we determined the size of the backwards window to calculate the history force integral. According to the model of the history force used in the present work, in which this force is acting during slow radial and translational dynamics, we start the analysis in a fix time when the bubble has a maximum radius and is when the history force will act. In Fig.(3) we show the previous dynamics of an Argon bubble in SA85 with $R_0 = 9.0\mu m$ and forced by $p_a^0 = 1.65$ bar at $f_0 = 30$ kHz. Fig.(3) also shows how the value of the x-component of the history force (without the switches), at the time when the bubble has the maximum radius, changes with the amount of time backwards considered to make the calculation. It can be seen that the contribution of this force at any given time is finite. In addition, the very first previous points have the biggest weight and then the biggest contributions to the history force. The variation of $\frac{d(RU_x)}{dt}$ is also displayed in the lower panel of Fig.(3). It can be seen that during a 400 points window the variations are small compared with the variations at main collapse, first and second rebound. With this size of window we are allowed to research the $R_0 = [3.0; 12.0]\mu m$ and $p_a^0 = [1.2; 2.7]$ bar parameter phase space for Argon bubbles in SA85, because the criteria of small variations within the window is conserved.

Property	Value
Density ρ_l	$1778.6 \frac{kg}{m^3}$
Dynamic viscosity μ_l	$0.015 Pa.s$
Kinematic viscosity ν_l	$8.4 \times 10^{-6} \frac{m^2}{s}$
Speed of sound c_l	$1473.0 \frac{m}{s}$
Vapor pressure p_v	$2.45 Pa$
Surface tension σ	$0.074 \frac{N}{m}$

Table 1: Properties at 20°C of Sulfuric acid solution $SO_4H_2(85\% \text{ wt}) - H_2O(15\% \text{ wt})$. Poling et al. (2008) and Young and Grinstead (1949)

3 HYDRODYNAMIC FORCES DURING A RADIAL CYCLE

A typical simulation made with the present model implies the calculation of 10000 radial cycles of the bubble. In this section we focus on the description of main variables in a time scale imposed by the ultrasound, typically $T = \frac{1}{f_0} \simeq 33\mu s$. We considered as a base case an Argon bubble in SA85 driving at $f_0 = 30.0$ kHz with $p_a^0 = 1.65$ bar and an amount of non-condensable gas equivalent to $R_0 = 9.0\mu m$. The liquid properties used in the proposed model are listed in Table(1). In Fig.(4) the radius of the bubble as a function of time can be seen. It is also shown that from the bubble ambient radius up to the maximum radius, the Péclet number is $Pe \ll 1$, which implies that the non-condensable gas inside the bubble follows an isothermal evolution. During the main collapse and rebounds, the $Pe \gg 1$ and the gas follows a polytropic evolution. The temperature computed by this model is also shown. It can be seen that during main collapse the gas temperature reaches 18300 K. The inset in Fig.(4B) shows that during the expansion phase, the non-condensable gas is in thermal equilibrium with the liquid at $T_l = 293.15$ K. In Fig.(5) the module of each force acting on the bubble as the radius of the bubble varies in response to the forcing acoustic field can be seen. In all cases we show the buoyant force to

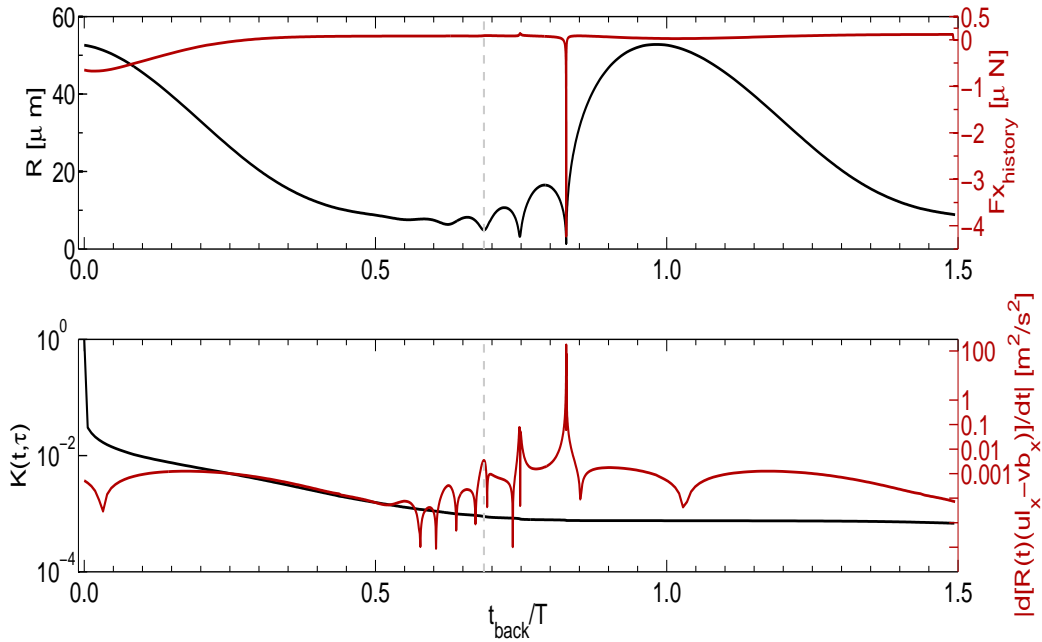


Figure 3: (upper panel) The solid black line is the radius of the bubble at previous times calculated with the numerical model considering the coupling between the radial and translational dynamics but without the feedback of the history force. The red line is the history force in the x-direction on the bubble at maximum expansion ($t_{back} = 0$) calculated with different numbers of points backwards. The parameters of the Argon bubble in SA85 are: $R_0 = 9.0\mu m$ and $p_a^0 \simeq p_a^b = 1.65$ bar at $f_0 = 30.0$ kHz. (lower panel) The solid black line indicates the value of the kernel approximated by Ren-Mackenzie form in logarithmic scale. With red line is shown the absolute value of $\frac{d[R(t)\vec{U}_x(r,t)]}{dt}$ in logarithmic scale. For the time interval defined by 400 points backwards, indicated with gray dotted line, the variations of $\frac{d[R(t)\vec{U}_x(r,t)]}{dt}$ are rather small compared with the variation during main collapse. The variations are lower than 0.01% from the mean value. During this time interval the “window model” used to calculate the history force is valid according to [Dorgan and Loth \(2007\)](#). This analysis is similar for the y-direction and z-direction.

compare the magnitudes. Although the Bjerknes force is responsible for the trapping of this size of bubble in the antinode, it is the force with the smallest magnitude of all and it is minimum during main collapse. The added mass force is maximum during main collapse and so is the steady drag force. Regarding the history force it can be seen that is null during main collapse and it will act when the bubble is in the expansion phase and during each maximum of the bubble rebounds. The latter is best illustrated in Fig.(6) which shows how the switches turn on and turn off the action of the history force during the radial cycle. Also the characteristic Reynolds numbers of the problem are displayed in comparison with the thresholds values of the model that controls the switches of the history force. The maximum values of $Re_t = 17$ and $Re_r = 180$ occurs during main collapse. It can be seen that during most of the time the $Re_t < 1$ is less than the unit. This is in agreement with the validity range of the Stokes-like drag solution used in the present model. Fig.(7) shows that the maximum translational displacement of the bubble occurs at the time of main collapse and rebounds of the radial cycle. This coincides with sudden growth of added mass force and drag force in agreement with the results of [Sadighi-Bonabi et al. \(2009\)](#). It can be seen that the maximum force applied on the bubble during main collapse reaches $|\vec{F}_b| = 400\mu N$.

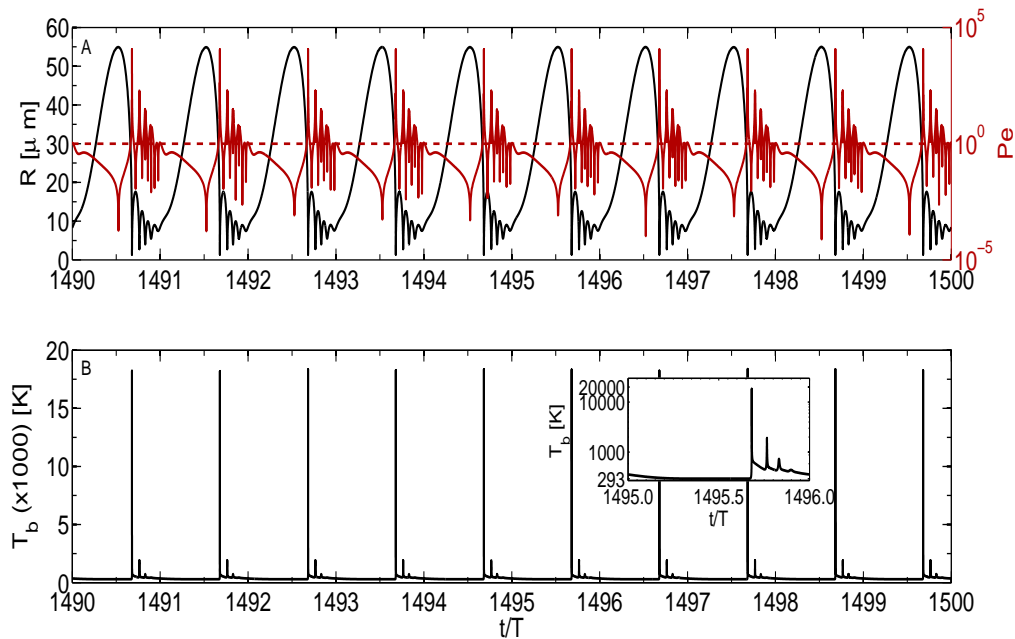


Figure 4: (A) In black is shown the radius as function of time of an Argon bubble in SA85. $R_0 = 9.0\mu\text{m}$ and $p_a^0 = 1.65$ bar driven at $f_0 = 30$ kHz. In red is shown the Pe number. The red dotted line indicates $Pe = 1$. During the expansion phase up to maximum radius the $Pe \ll 1$ and the gas inside the bubble follows an isothermal evolution ($\gamma \simeq 1$). During main collapse and rebounds the $Pe \gg 1$ and the gas inside the bubble follows a polytropic evolution until adiabatic. As $Pe \rightarrow \infty$ the polytropic coefficient tends to the adiabatic coefficient $\gamma \rightarrow \Gamma$. (B) Temperature of the gas inside the bubble. The inset shows that the gas is in thermal equilibrium with the liquid ($T_l = 293.15$ K) during the expansion phase up to main collapse.

4 HYDRODYNAMIC FORCES AT LONG TIMES

In this section we show the results in a longer time scale. We have seen that the translational displacement of the bubble is of the order of $\sim \mu\text{m}$ per radial cycle. To be able to see typical translational displacement of the order of $\sim \text{mm}$ we made the simulations over 10000 radial cycles. Fig.(8) shows the simulated m-SBSL state of an Argon bubble in SA85 driven at $p_a^0 = 1.65$ bar at $f_0 = 30.0$ kHz with an amount of gas equivalent to $R_0 = 9.0\mu\text{m}$. The initial conditions for the bubble position are very close to the origin of coordinates (center of the resonator). We made several tests and the shape of pseudo-orbits obtained can vary with the initial conditions of bubble position under the same driving parameters. It can be seen that the final mean levitation position is over the pressure antinode. If the initial condition of the bubble position is beneath the pressure antinode, the bubble will translate to a final position above describing a larger path to it. We applied the fft algorithm to $x(t)$, $y(t)$ and $z(t)$ to determine the characteristic oscillation frequency. In Fig.(9) we show the normalized amplitude spectrum for the three directions. The peaks in the $x(t)$ and $y(t)$ occur at a frequency of 70 Hz, while in the $z(t)$ direction the frequency of the oscillations is 42 Hz. For low frequencies in the $z(t)$ direction it can be seen a growth in the spectrum associated with the shifted levitation location from antinode.

From Eq.(10) it can be seen that all forces are tangent at every point of the trajectory except the Bjerknes force. In Fig.(10) the directions of the Bjerknes force and history force along the bubble trajectory for the first 1500 radial cycles of the case in Fig.(8) are shown. The values are averaged in each radial cycle. The Bjerknes force acts like a centripetal force directed towards

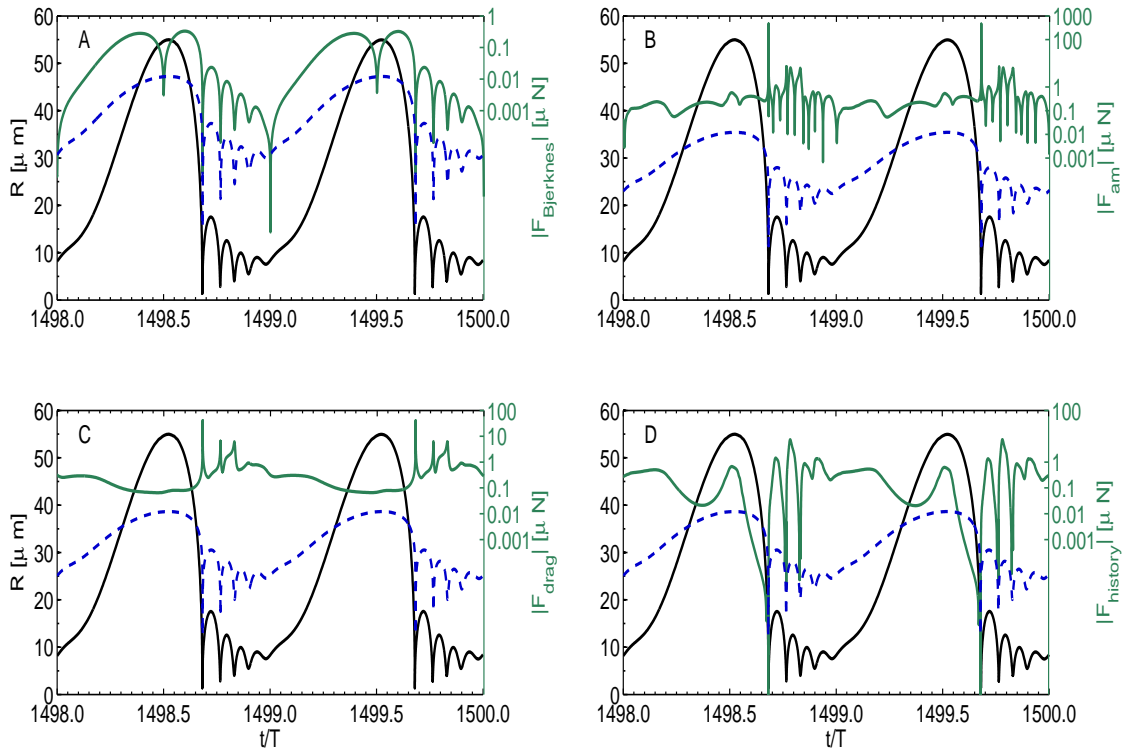


Figure 5: (black) Radius as function of time of an Argon bubble in SA85. $R_0 = 9.0\mu m$ and $p_a^0 = 1.65$ bar driven at $f_0 = 30$ kHz. (green line) (A) Bjerknes force module.(B) Added mass force module. The maximum value during main collapse is $|F_{am}| = 460\mu N$.(C) Quasi-steady drag force module. The maximum value during main collapse is $|F_d| = 40\mu N$. (D) History force module. (blue dotted line) Buoyant force module.

the antinode. In Fig.(11) the relative angle between the trajectory and the Bjerknes force can be seen. When the bubble turns around the angle is almost 180° while if the bubble path is nearly straight the angle decreases.

In Fig.(12) we show the module of each force averaged in each radial period. The Bjerknes force varies within 33.3% over the 10000 radial cycles, while the added mass force oscillates within 11%. The steady drag force oscillates in a narrow range within 5% and so does the history force.

In Fig.(13) we show the variation of some interesting parameters from the point of view of energy concentration along the bubble path. We show that the maximum temperature achieved by the non-condensable gas inside the bubble during main collapse predicted by this model varies within a 3% around 18000 K. Moreover, the compression ratio has small oscillations within 2%. This indicates that there is not a spatial region along the bubble path in which a significant increment of temperature can be reached. The instant of main collapse when the bubble interface acquires the maximum radial velocity is characterized by $Ma = 0.42$ in agreement with the radial model employed.

As it was shown, the bubble translates around a mean vertical displaced position from the resonator center. To evaluate the variations of the acoustic pressure at bubble position while it is translating, we follow Urteaga et al. (2007). In Fig(14) it can be seen that the acoustic pressure at bubble position is slightly lower than the acoustic pressure at the central pressure antinode of the acoustic field and varies within 1500 Pa.

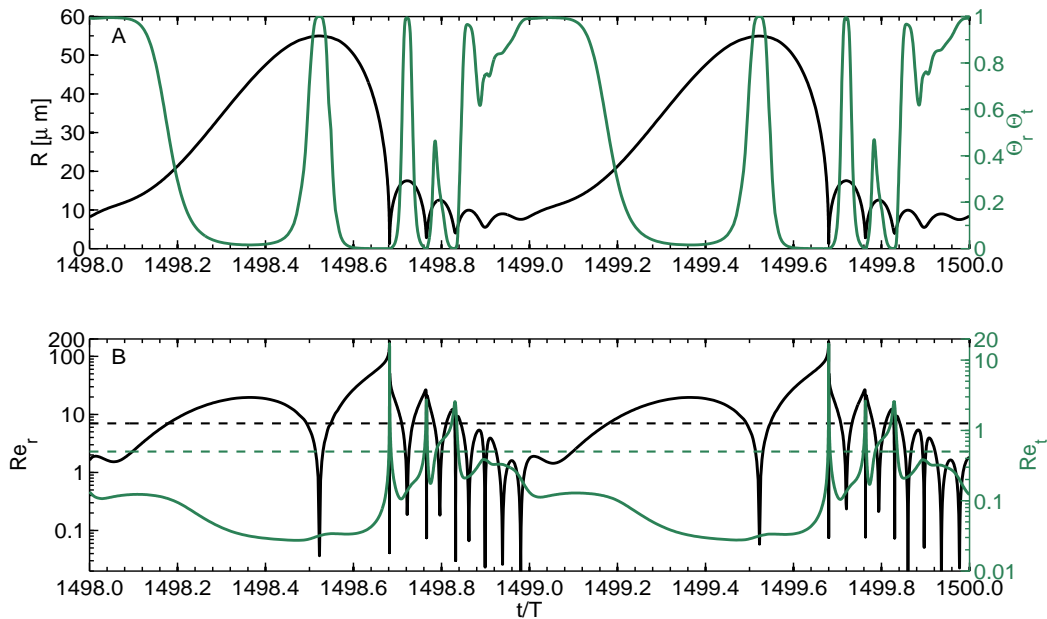


Figure 6: (A) (black) Radius of the bubble as function of time of an Argon bubble in SA85. $R_0 = 9.0\mu\text{m}$ and $p_a^0 = 1.65$ bar driven at $f_0 = 30$ kHz. (green) The turn on/off of the history force given by the switches $\theta_r(t)$ and $\theta_t(t)$. (B) (black) Re_r is over the threshold value during the expansion phase and during the Rayleigh-Plesset collapse. (green) Re_t is only over the threshold during main collapse and during rebounds.

5 POSITIONAL STABILITY

The spatial shifting of the mean levitation position of an Argon bubble in SA85 as the amplitude of driving pressure increases is numerically analyzed. This experimental fact was reported by Urteaga et al. (2007) and indicated that it is a limiting factor on the maximum acoustic pressure that can be applied to the bubble.

In Fig.(15) the trajectories of an Argon bubble with $R_0 = 9.0\mu\text{m}$ in SA85 driving at $f_0 = 30\text{kHz}$ are shown. For pressure amplitudes at the resonator center lower than $p_a^0 < 1.30$ bar no pseudo-orbits appear and the bubble remains fixed in a stable position above the center of coordinates. For $p_a^0 > 1.32$ bar the bubble translates around a mean position, which shifts towards a bigger radius as the amplitude of the driving pressure rises. A remarkable change in the shape of the pseudo-orbits can be seen for $p_a^0 > 1.70$ bar. In Fig.(16) we display the results for amplitudes of acoustic pressures beyond $p_a^0 > 1.65$ bar. It is shown that the pseudo-orbits are wider on a spherical gasket as the amplitude of the driving pressure is more intense. Fig.(17) shows the mean levitation position of the bubble for the range of simulations displayed in Fig.(15) and Fig.(16) as function of the amplitude of the driving pressure at the resonator center.

All the forces acting on the bubble were computed for the simulations shown in Fig.(17). In Fig.(18), we show the Bjerknes force, drag force and history force averaged in a radial cycle, as well as the maximum value of the module of the added mass along 10000 radial cycles for different pressures at the resonator center. Different behaviors exist when the driving pressure rises. For $p_a^0 > 1.32$ bar there exists a small transition gap where oscillations in each magnitude are present. As the driving pressure rises, it can be seen from Fig.(18A) that the averaged Bjerknes force is more intense, and its magnitude is comparable with the averaged history force (See Fig.(18D)).

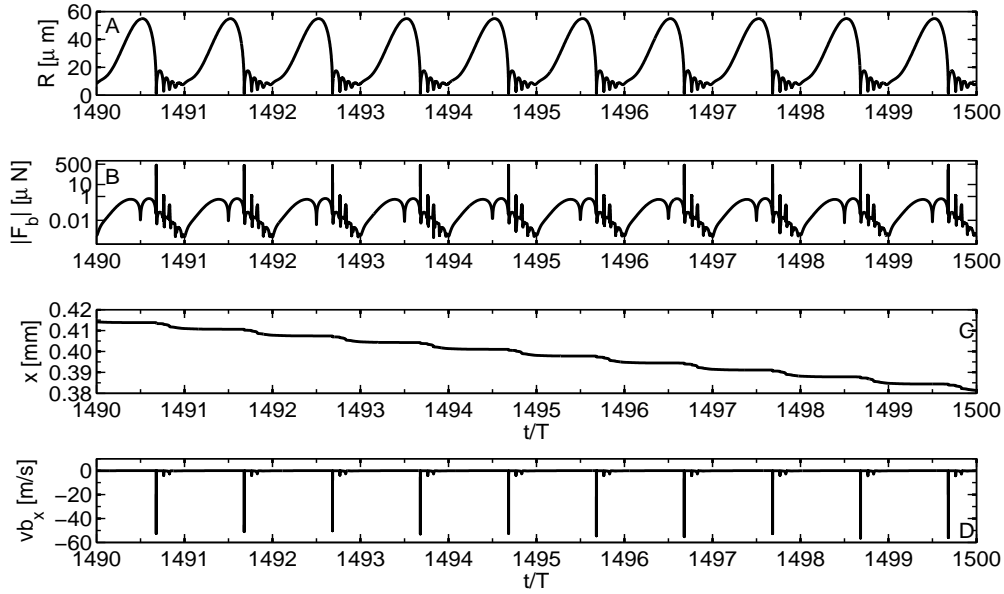


Figure 7: (A) Radius of the bubble as function of time of an Argon bubble in SA85. $R_0 = 9.0\mu m$ and $p_a^0 = 1.65$ bar driven at $f_0 = 30$ kHz. (B) Magnitude of the net force acting on the bubble. Due to the delfiform growth of the added mass force and drag force, the main translational displacement of the bubble occurs during main collapse and rebounds of the radial dynamics. (C) Translation in the x-coordinate. Analogous behavior occurs for the other components. In this particular case, a typical translation distance per radial cycle is $\sim 3\mu m$. (D) Translational velocity of the bubble in the x-component. During most of the time of the radial cycle the translational velocity ranges between $\sim 1\frac{mm}{s}$ and $\sim 100\frac{mm}{s}$, except on main collapse when a sudden growth of translational velocity during several nanoseconds is observed.

6 COMPARISON WITH THEORETICAL SOLUTION AT SMALL ACOUSTIC PRESSURES

Morrison and Stewart (1976) developed a theoretical solution for the equation of motion of a bubble moving relative to an accelerating liquid. In their formulation they assumed a fix radius of the bubble which is subjected to a sinusoidally oscillating liquid. They solved the steady-state bubble response by transforming the translational equation into the Fourier space. Furthermore, the ratio between the transformed bubble velocity \tilde{v}_b and transformed liquid velocity \tilde{u}_l is:

$$\frac{\tilde{v}_b}{\tilde{u}_l} = \frac{\left[\frac{2}{3} + 2\sqrt{\frac{\Omega}{2}} - 3\Omega\sqrt{\frac{\Omega}{2}} \right] + i \left[3\Omega + 2\sqrt{\frac{\Omega}{2}} + 3\Omega\sqrt{\frac{\Omega}{2}} \right]}{\left[\frac{2}{3} + 2\sqrt{\frac{\Omega}{2}} - \Omega\sqrt{\frac{\Omega}{2}} \right] + i \left[\Omega + 2\sqrt{\frac{\Omega}{2}} + \Omega\sqrt{\frac{\Omega}{2}} \right]} \quad (14)$$

In Eq.(14), $\Omega = \frac{R_0^2 2\pi f_0}{9\nu_l}$ is the dimensionless frequency, and the phase ϕ between the bubble velocity and the liquid velocity is given by:

$$\phi = \text{Arctg} \left[\frac{\text{Im}(\frac{\tilde{v}_b}{\tilde{u}_l})}{\text{Re}(\frac{\tilde{v}_b}{\tilde{u}_l})} \right] \quad (15)$$

We compared the numerical model with this theoretical solution but the range of validity is only for small acoustic pressures (less than Blake threshold) applied to the bubble because in

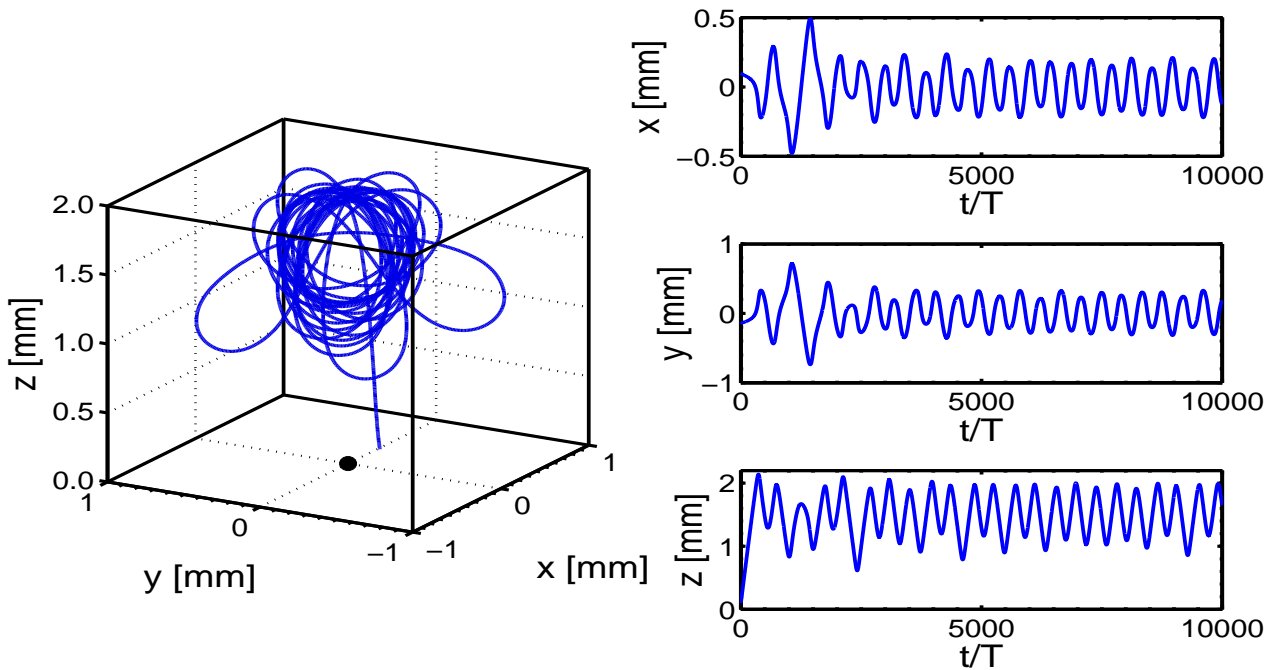


Figure 8: m-SBSL state of an Argon bubble in SA85 with an amount of gas $R_0 = 9.0\mu\text{m}$ and driving at $p_a^0 = 1.65$ bar at $f_0 = 30.0$ kHz. The initial conditions for the ODE system are: $R_i = R_0$, $\dot{R}_0 = 0.0\frac{\text{m}}{\text{s}}$, $T_b^0 = T_l$, $x_0 = 0.1$ mm, $\dot{x}_0 = 0.0\frac{\text{m}}{\text{s}}$, $y_0 = -0.15$ mm, $\dot{y}_0 = 0.0\frac{\text{m}}{\text{s}}$, $z_0 = 0.1$ mm, $\dot{z}_0 = 0.0\frac{\text{m}}{\text{s}}$. The simulation was made during 10000 radial cycles. For these particular parameters the bubble levitates in a mean position $x_m = 0.0$ mm, $y_m = 0.0$ mm, $z_m = 1.5$ mm above the pressure antinode. The black point indicates the origin of coordinates.

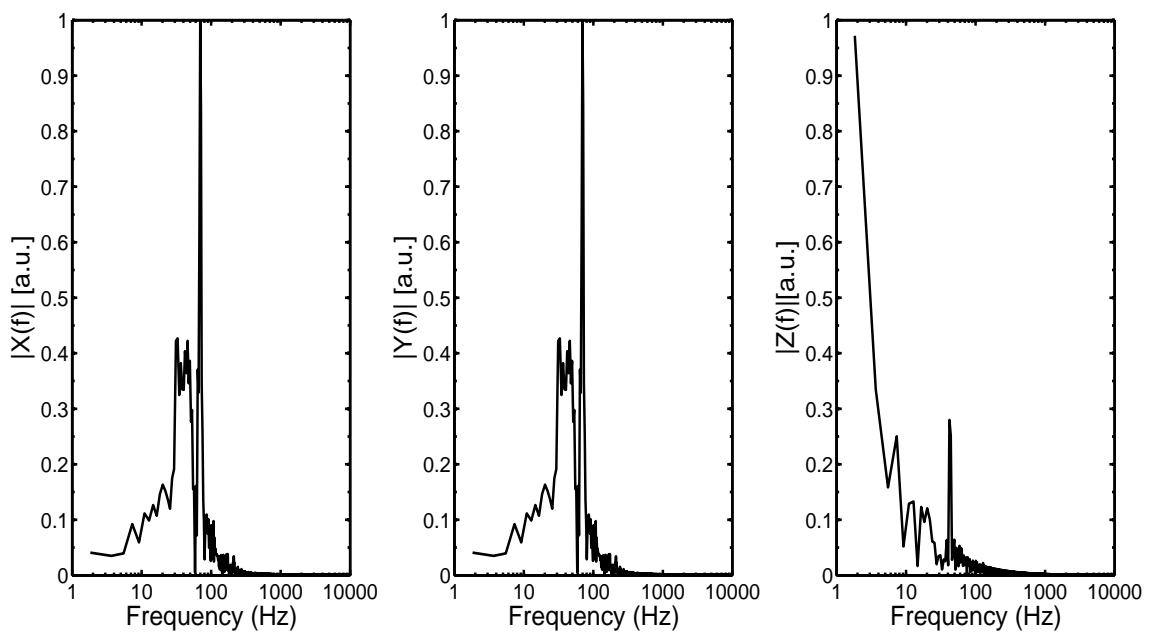


Figure 9: Normalized amplitude spectrum of $x(t)$, $y(t)$, $z(t)$ of the case in Fig.(8). The frequency of the oscillations in $x(t)$ and $y(t)$ is 70 Hz while in $z(t)$ is 42 Hz.

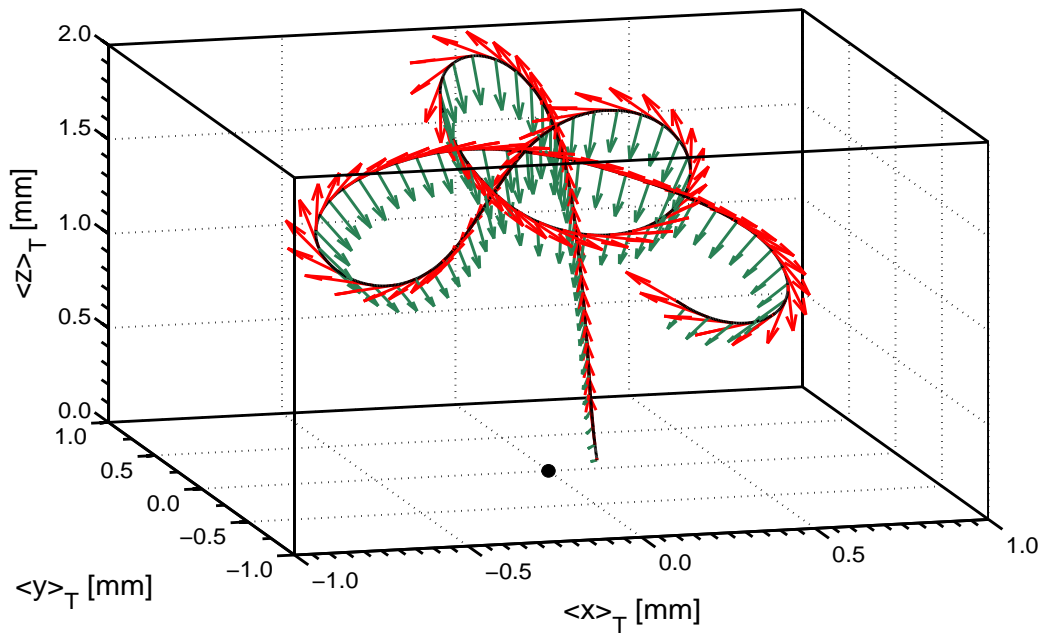


Figure 10: Direction of the $F_{history}$ (red) and $F_{Bjerknes}$ (green) for an Ar bubble in SA85 for the first 1500 radial cycles. $R_0 = 9.0\mu m$ and $p_a^0 = 1.65$ bar. The initial conditions for the bubble are: $x_0 = 0.1$ mm, $\dot{x}_0 = 0.0 \frac{m}{s}$, $y_0 = -0.15$ mm, $\dot{y}_0 = 0.0 \frac{m}{s}$, $z_0 = 0.1$ mm, $\dot{z}_0 = 0.0 \frac{m}{s}$. (black) Trajectory of the bubble. The Bjerknes force is the only force that is not tangent at every point of the trajectory and is responsible of trapping the bubble near the pressure antinode. The history force is always tangent to the trajectory.

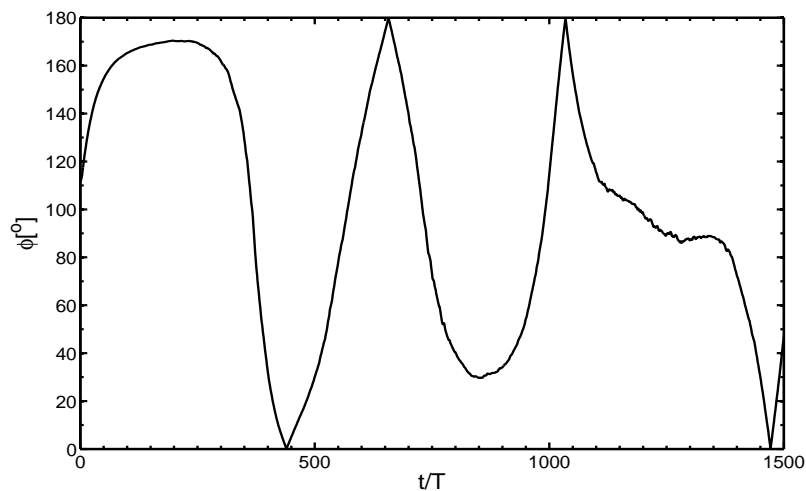


Figure 11: Angle between the vector of $F_{Bjerknes}$ and the vector tangent to the trajectory for the case of Fig.(10). At every turn of the bubble trajectory the angle increase up to 180° . When the trajectory of the bubble is almost straight the angle decreases.

this circumstance the response of the bubble is linear. Fig.(19) shows the magnitude of the ratio between velocities and the phase for an Argon bubble $R_0 = 5.0\mu m$ in SA85 under an applied acoustic pressure of $p_a^0 = 0.01$ bar. It can be seen that for low dimensionless frequency the bubble follows the movement of the liquid, and as the driving frequency rises the bubble advances the liquid. In the typical range of driving frequencies used in SBSL indicated with

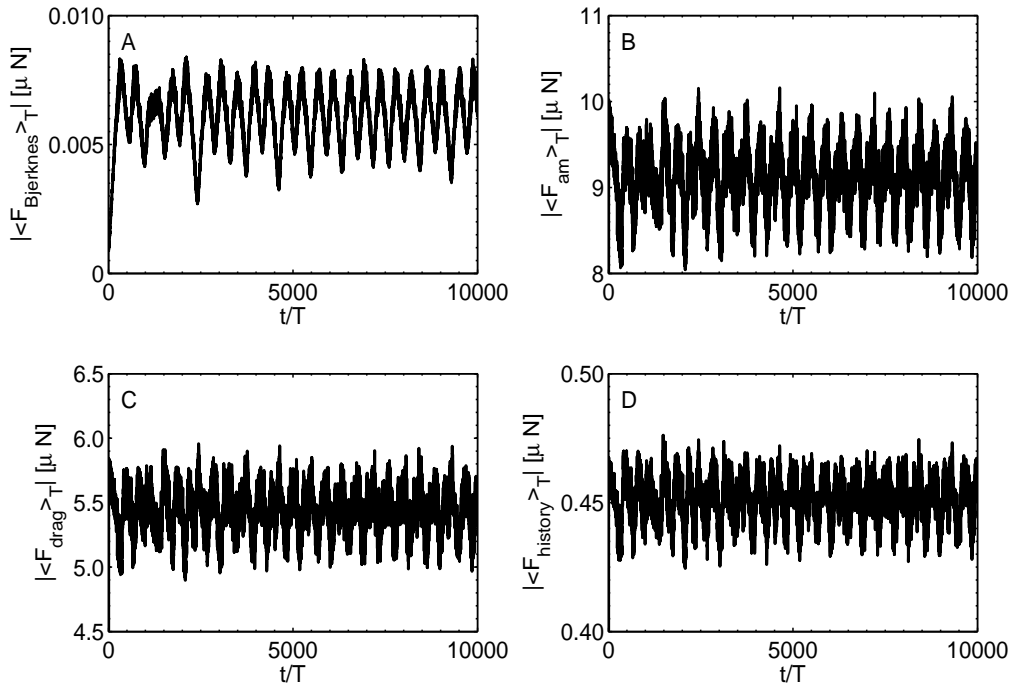


Figure 12: (A) Module of the Bjerknes force averaged in each radial cycle. (B) Module of the added mass force averaged in each radial cycle. (C) Module of the steady drag force averaged in each radial cycle. (D) Module of the history force averaged in each radial cycle.

gray dotted lines the agreement is quite good.

7 SIMULATIONS IN ETHYLENE GLYCOL

With the present model we made simulations of an Argon bubble in Ethylene Glycol as a check of consistency. In this section we show the simulation of two cases of the phase space reported by [Toegel et al. \(2006\)](#). In his work he indicated that a bubble in Ethylene Glycol with an amount of gas equal to $R_0 = 20.0\mu m$ driving by $p_a^0 = 1.40bar$ at $f_0 = 23kHz$ is shape stable and path unstable. The bubble trajectory for this case is shown in [Fig.\(20\)](#).

With the same argument as in the sulfuric acid case, the size of the window to calculate the history force on a bubble in Ethylene Glycol is $N = 500$ points backwards. The liquid properties used in the simulation are listed in [Table.\(2\)](#). It can be seen in [Fig.\(20\)](#) that the transient time extends during 5000 radial cycles after the bubble reaches a nearly periodic movement around a point located 0.5 mm above the origin of coordinates.

On the other hand, if the forcing pressure is diminished up to $p_a^0 = 1.10 bar$, [Toegel et al. \(2006\)](#) calculations predict that a bubble is shape stable and also path stable. This indicates that no pseudo-orbits are described by the bubble. This last case is shown in [Fig.\(21\)](#). It can be seen that the bubble translates to a final position above the pressure antinode without making pseudo-orbits.

8 CONCLUSIONS

We have presented a numerical implementation which describes the coupling between the radial and translational dynamics of a periodically excited bubble located in a spherical pressure field.

Property	Value
Density ρ_l	1100.0 $\frac{kg}{m^3}$
Dynamic viscosity μ_l	0.022 Pa.s
Kinematic viscosity ν_l	$20.0 \times 10^{-6} \frac{m^2}{s}$
Speed of sound c_l	1660.0 $\frac{m}{s}$
Vapor pressure p_v	13.3 Pa
Surface tension σ	0.045 $\frac{N}{m}$

Table 2: Properties of Ethylene Glycol Toegel et al. (2006)

No approximations were made on the pressure field in this work. We characterized all the forces acting on the bubble in the radial scale and during several periods until we could observe the typical pseudo-orbits described by the bubble in a highly viscous fluid as sulfuric acid solution at 85% w/w. Special attention was paid to the inclusion of the history force to the scheme. We used a suitable different approximation of the kernel of the history force model and applied the window method. The main advantage of the present implementation in comparison to previous numerical schemes, is that it allows the calculation of the history force at each time instant. We have shown that the numerical implementation reproduced experimental facts in the range of parameters reported in the literature. This implementation will allow a deeper study of the path instability of bubbles in viscous liquids.

ACKNOWLEDGMENTS

L.M.R. and D.H.D. were financed by CONICET.

REFERENCES

- Akhatov I., Mettin C., Ohl D., Parlitz U., and Lauterborn W. "Bjerknes force threshold for stable single bubble sonoluminescence.". *Phys. Rev. E*, 55:3747–3750, 1997.
- Batchelor G. "An introduction to fluid dynamics". Cambridge University Press, 1967.
- Dellavale D. "Concurrent signal processing algorithms with applications in sonoluminescence". Ph.D. thesis, Instituto Balseiro. Univ. Nac. Cuyo, 2012.
- Dellavale D., Rechimán L., Rosselló J., and Bonetto F. "Upscaling energy concentration in multifrequency single-bubble sonoluminescence with strongly degassed sulfuric acid.". *Phys. Rev. E*, 86:016320, 2012.
- Didenko Y., McNamara W.B., and Suslick K. "Molecular emission during single bubble sonoluminescence.". *Nature*, 407:877–879, 2000.
- Dorgan A. and Loth E. "Efficient calculation of the history force at finite Reynolds numbers.". *Int. J. Multiphase Flow*, 33:833–848, 2007.
- Flannigan D. and Suslick K. "Plasma formation and temperature measurement during single-bubble cavitation.". *Nature (London)*, 434:52–55, 2005.
- Gaitan D., Crum L., Church C., and Roy R. "Sonoluminescence and bubble dynamics for a single, stable, cavitation bubble.". *J. Acoust. Soc. Am.*, 91:3166–3183, 1992.
- Galavani Z., Rezaei-Nasirabad R., and Bhattarai S. "On the dynamics of moving single bubble sonoluminescence.". *Phys. Letters A*, 374:4531–4537, 2010.
- Hilgenfeldt S., Grossmann S., and Lohse D. "Sonoluminescence light emission". *Phys. Fluids*, 11:1318–1330, 1999.
- Hopkins S., Putterman S., Kappus B., Suslick K., and Camara C. "Dynamics of a Sonolumi-

- nescing Bubble in Sulfuric Acid.*" *PRL*, 95:254301, 2005.
- Keller J. "Bubble oscillations of large amplitude". *J. Acoustic Soc. Am.*, 68:628–633, 1980.
- Leighton T. "The acoustic bubble". Academic Press, 1994.
- Magnaudet J. and Legendre D. "The viscous drag force on a spherical bubble with a time-dependent radius.". *Phys. Fluids*, 10:550–554, 1998.
- Mei R., Klausner J., and Lawrence C. "A note on the history force on a spherical bubble at finite Reynolds number.". *Phys. Fluids*, 6:418–420, 1994.
- Mirheydari M., Sadighi-Bonabi R., Rezaee N., and Ebrahimi H. "Optimization of the bubble radius in a moving single bubble sonoluminescence.". *Physica Scripta*, 83:055403, 2011.
- Morrison F. and Stewart M. "Small bubble motion in an accelerating liquid.". *J. Appl. Mech.*, 43:399–403, 1976.
- Poling B., Thomson G., Fried D., Rowley R., and Wilding W. "Perry's Chemical Engineers' Handbook. Section 2: Physical and Chemical Data", volume 8th Edition. McGraw Hill, 2008.
- Press W., Teukolsky S., and Vetterling W. "Numerical Recipes in C: The art of scientific computing". Cambridge University Press, 1992.
- Puente G. and Bonetto F. "Proposed method to estimate the liquid-vapor accommodation coefficient based on experimental sonoluminescence data.". *Phys. Rev. E*, 71:056309, 2005.
- Ren C. and MacKenzie A. "Closed-form approximations to the error and complementary error functions and their applications in atmospheric science". *Atmospheric Science Letters*, 8:70–73, 2007.
- Sadighi-Bonabi R., Mirheydari M., Rezaee N., and Ebrahimi H. "Effects of fluid viscosity on a moving sonoluminescing bubble.". *Phys. Rev. E*, 84:026301, 2011.
- Sadighi-Bonabi R., Rezaei-Nasirabad R., and Galavani Z. "The dependence of the moving sonoluminescing bubble trajectory on the driving pressure.". *J. Acoustic Soc. Am.*, 126:2266–2272, 2009.
- Toegel R., Luther S., and Lohse D. "Viscosity destabilizes sonoluminescing bubbles.". *PRL*, 96:114301/1–114301/4, 2006.
- Urteaga R. and Bonetto F. "Trapping an Intensely Bright, Stable Sonoluminescing Bubble.". *PRL*, 100:074302, 2008.
- Urteaga R., Dellavale D., Puente G., and Bonetto F. "Positional stability as the light emission limit in sonoluminescence with sulfuric acid.". *Phys. Rev. E.*, 76:056317, 2007.
- van Hinsberg M., ten Thije Boonkkamp J., and Clercx H. "An efficient, second order method for the approximation of the Basset history force.". *J. Comp. Phys.*, 230:1465–1478, 2011.
- Yang S. and Leal L. "A note on memory-integral contributions to the force on an accelerating spherical drop at low Reynolds number.". *Phys. Fluids*, 3:1822–1824, 1991.
- Young T. and Grinstead S. "The surface tensions of aqueous sulfuric acid solutions.". *Annals New York Academy of Science*, 51:765–780, 1949.

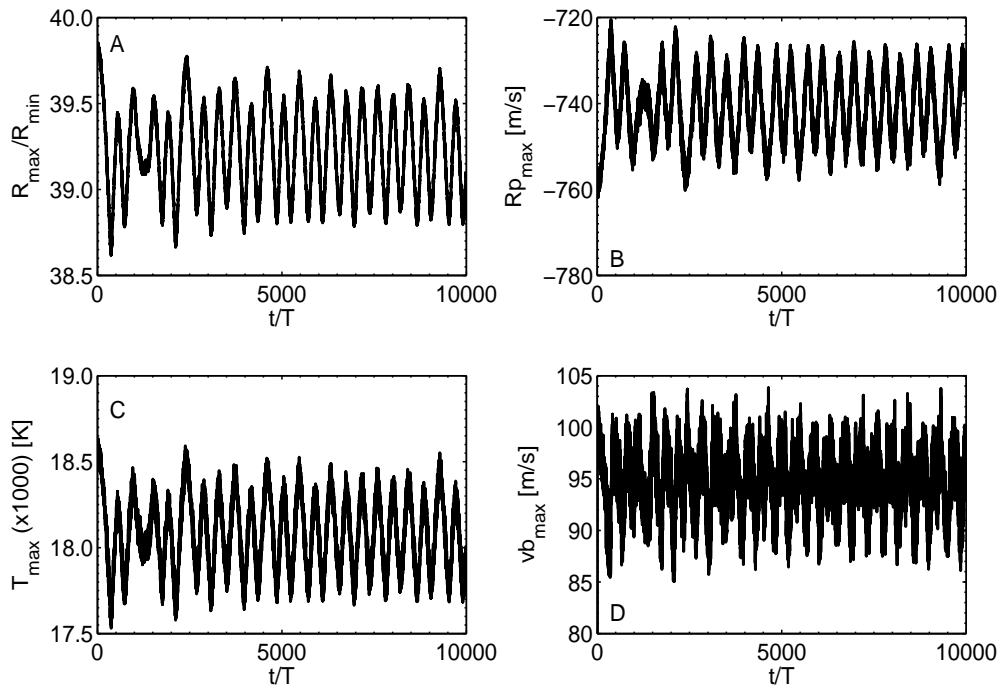


Figure 13: (A) Compression ratio for each radial cycle. (B) Maximum radial velocity at main collapse for each radial cycle. (C) Maximum temperature achieved by the non-condensable gas inside the bubble in each radial cycle. (D) Module of the peak of the bubble translational velocity.

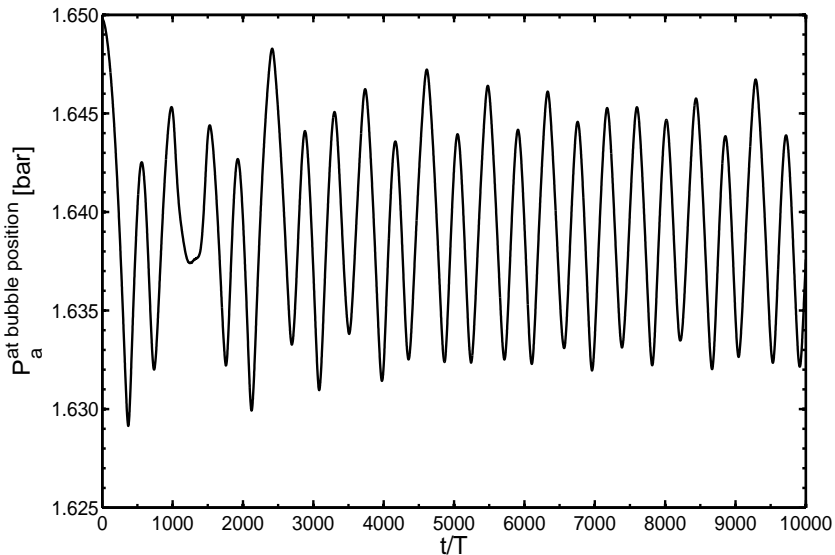


Figure 14: Pressure at bubble position given by [Urteaga et al. \(2007\)](#). It can be seen that the pressure applied on the bubble interphase while the bubble is translating varies within 1500 Pa.

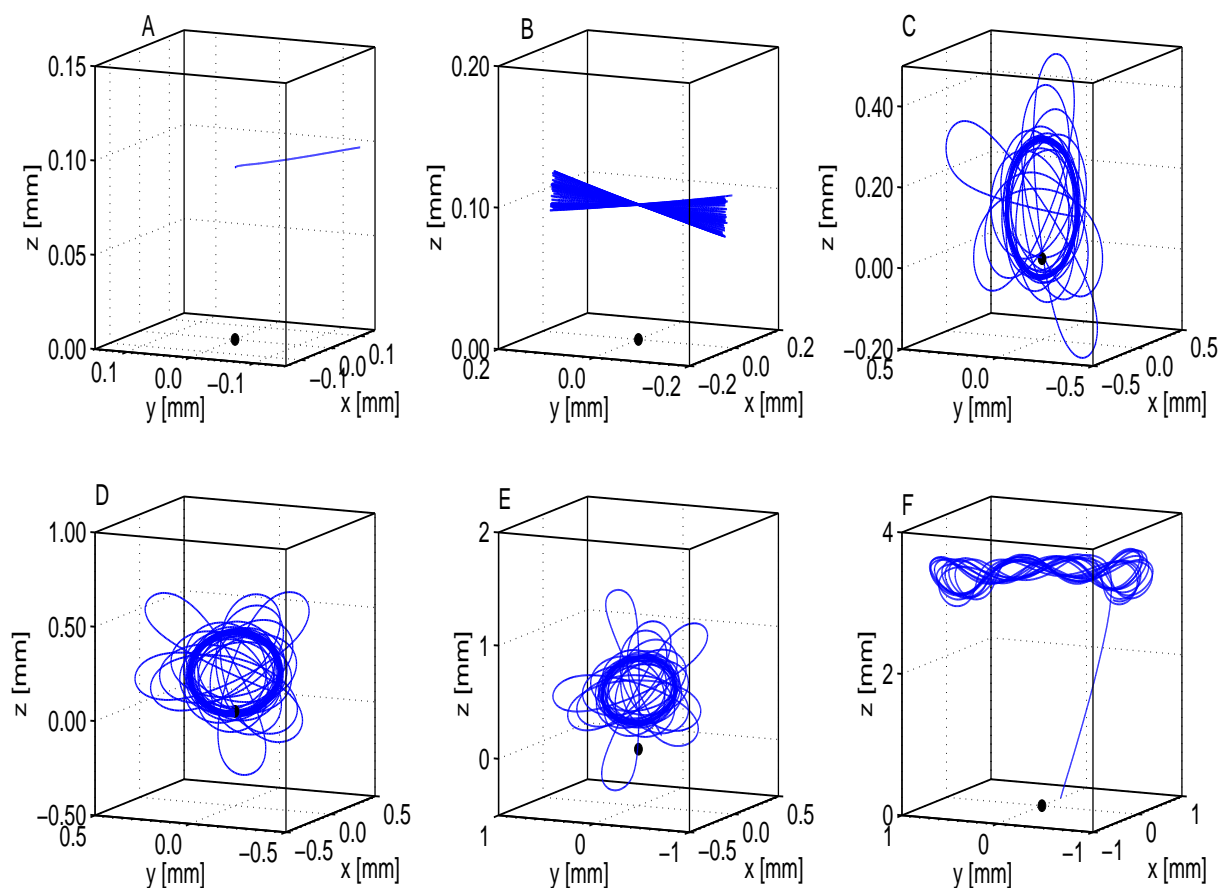


Figure 15: Simulations of an Argon bubble with $R_0 = 9.0\mu m$ in SA85 driving at $f_0 = 30kHz$ with different pressures amplitudes at the resonator center. (A) $p_a^0 = 1.30$ bar. (B) $p_a^0 = 1.32$ bar. (C) $p_a^0 = 1.40$ bar. (D) $p_a^0 = 1.50$ bar. (E) $p_a^0 = 1.60$ bar. (F) $p_a^0 = 1.70$ bar. The black dot indicates the origin of coordinates. The onset for the existence of pseudo-orbits is between $p_a^0 = 1.31$ bar and $p_a^0 = 1.32$ bar. As the amplitude of the driving pressure is increased the mean levitation positions shift upwards in the vertical direction. For each case 10000 radial cycles were solved.

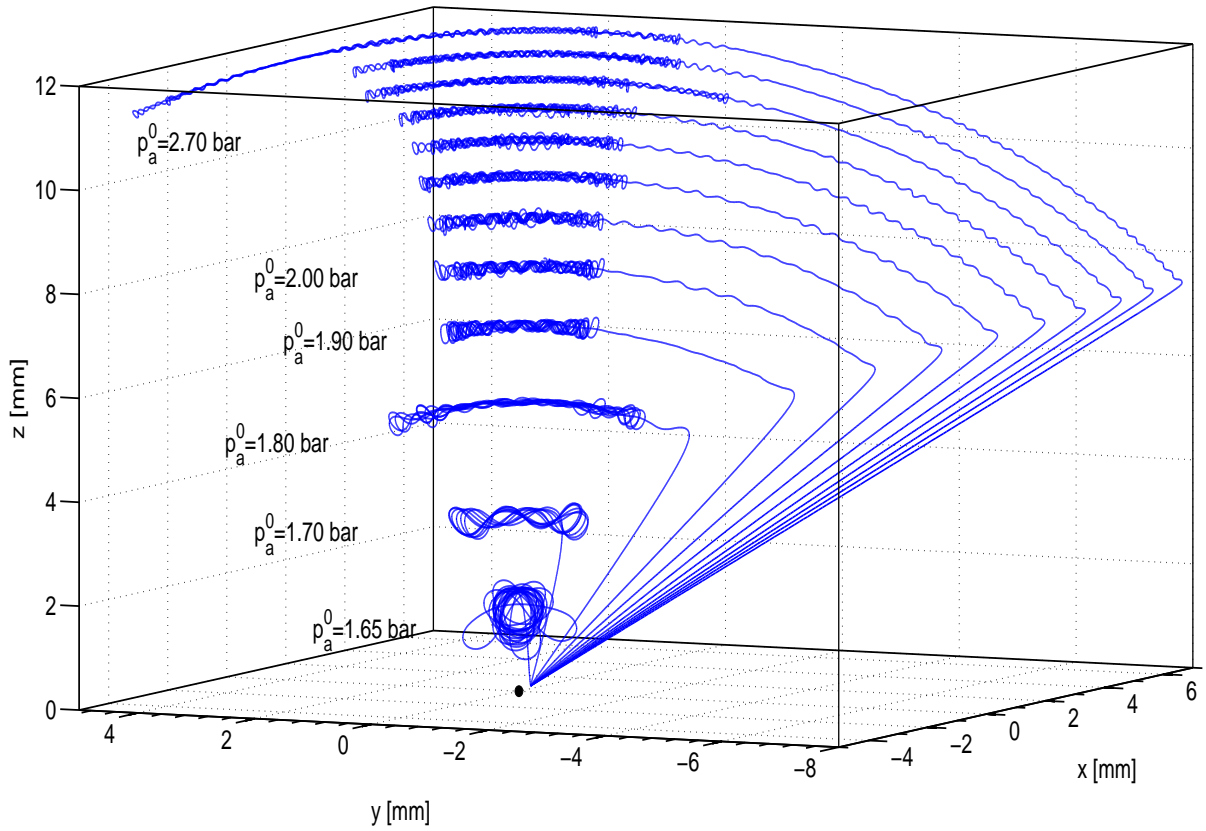


Figure 16: Simulations of an Argon bubble with $R_0 = 9.0\mu\text{m}$ in SA85 driving at $f_0 = 30\text{kHz}$ with different amplitude pressures: $p_a^0 = 1.65$ bar, $p_a^0 = 1.70$ bar, $p_a^0 = 1.80$ bar, $p_a^0 = 1.90$ bar, $p_a^0 = 2.00$ bar, $p_a^0 = 2.10$ bar, $p_a^0 = 2.20$ bar, $p_a^0 = 2.30$ bar, $p_a^0 = 2.40$ bar, $p_a^0 = 2.50$ bar, $p_a^0 = 2.60$ bar and $p_a^0 = 2.70$ bar. It can be seen a change in the structure of the orbits as the driving pressure rises. For each case 10000 radial cycles were solved.

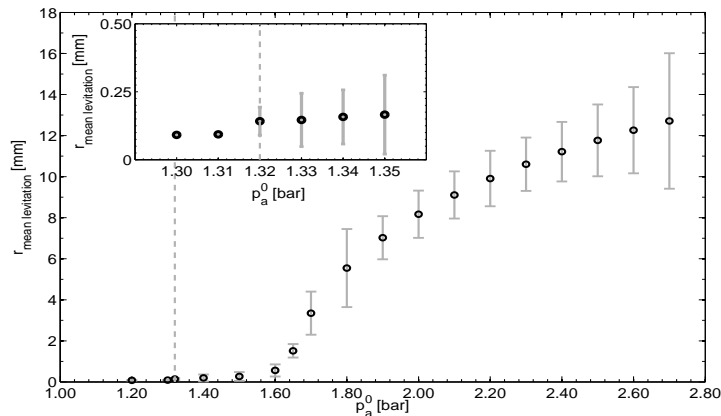


Figure 17: Mean levitation distance of an Argon bubble with $R_0 = 9.0\mu\text{m}$ in SA85 driving at $f_0 = 30\text{kHz}$ as function of the amplitude of the driving pressure at the resonator center. The gray bars indicate the approximate maximum amplitude of the pseudo-orbits. For driving pressures below $p_a^0 < 1.31$ bar no pseudo-orbits appeared. With dotted line is indicated the onset for the m-SBSL state at $p_a^0 = 1.32$ bar. The inset shows in detail the transition between the non-moving bubble and the moving-bubble.

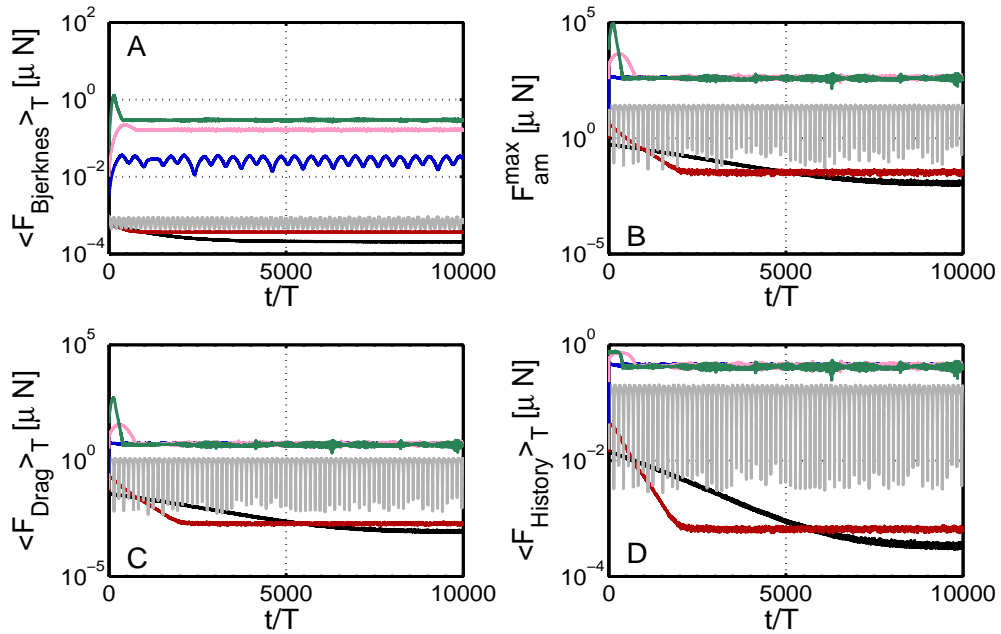


Figure 18: Force analysis during 10000 radial cycles for the simulations showed in Fig.(15), Fig.(16) and Fig.(17). (black) $p_a^0 = 1.20$ bar. (red) $p_a^0 = 1.30$ bar. (gray) $p_a^0 = 1.32$ bar, the onset of the moving state. (blue) $p_a^0 = 1.65$ bar. (pink) $p_a^0 = 2.00$ bar. (green) $p_a^0 = 2.70$ bar. (A) Bjerknes force module averaged in a radial cycle. As the pressure at the resonator center increases, the averaged Bjerknes force magnitude is more intense. (B) Maximum magnitude value of the added mass force. For the cases between $1.32 \text{ bar} < p_a^0 < 1.65$ bar, oscillations exist. For driving pressures higher than $p_a^0 > 1.65$ bar, the maximum value no longer increases and in the steady state it reaches approximately $|F_{am}^{max}| \sim 400 \mu N$. (C) Stokes-like drag force averaged in a radial cycle. The maximum value reached as the driving pressure rises is $\langle F_{drag} \rangle_T \sim 5 \mu N$. (D) History force averaged in a radial cycle. Oscillations exist when the bubble start to describe pseudo-orbits. The maximum mean value of the averaged history force as the driving pressure increases is $\langle F_{history} \rangle_T \sim 0.4 \mu N$. This magnitude is comparable to the averaged Bjerknes force module.

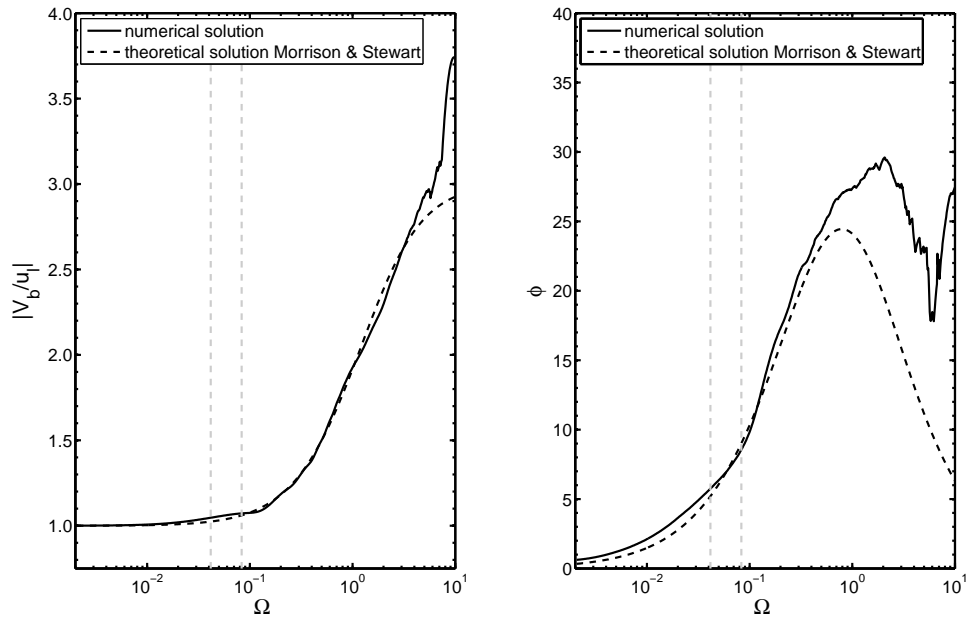


Figure 19: (left) Magnitude of the ratio of bubble velocity and liquid velocity. (right) Phase angle relative to liquid motion. The simulation was made for $R_0 = 5.0\mu\text{m}$ Argon bubble in SA85 under a static pressure of $p_0 = 0.92$ bar and excited with a low acoustic pressure $p_a^0 = 0.01$ bar where the bubble response is linear. The frequency sweeping was filtered using the Savitzky-Golay method with 15% span. (gray dotted line) Range of typical driving frequencies used in SBSL.

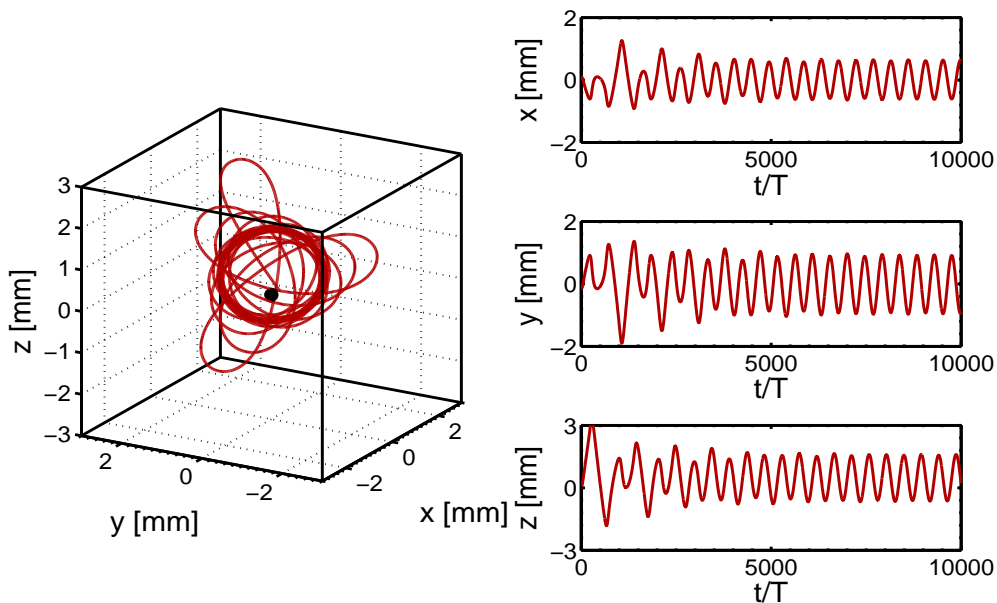


Figure 20: m-SBSL state of an Argon bubble in Ethylene Glycol with an amount of gas $R_0 = 20.0\mu\text{m}$ and driving with $p_a^0 = 1.40$ bar at $f_0 = 23.0$ kHz. The initial conditions for the ODE system are: $R_i = R_0$, $\dot{R}_0 = 0.0\frac{\text{m}}{\text{s}}$, $T_b^0 = T_l$, $x_0 = 0.10$ mm, $\dot{x}_0 = 0.0\frac{\text{m}}{\text{s}}$, $y_0 = -0.15$ mm, $\dot{y}_0 = 0.0\frac{\text{m}}{\text{s}}$, $z_0 = 0.10$ mm, $\dot{z}_0 = 0.0\frac{\text{m}}{\text{s}}$. The simulation was made during 10000 radial cycles. For these particular parameters the bubble levitates in a mean position $x_m = 0.0$ mm, $y_m = 0.0$ mm, $z_m = 0.5$ mm above the pressure antinode. The black point indicates the origin of coordinates.

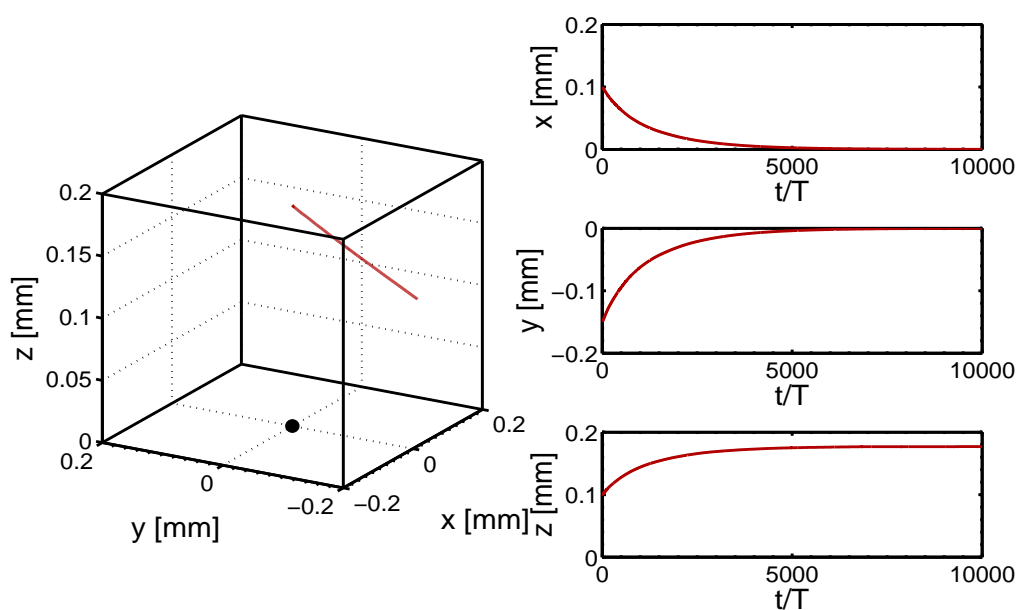


Figure 21: Argon bubble in Ethylene Glycol with an amount of gas $R_0 = 20.0\mu\text{m}$ and driving with $p_a^0 = 1.10$ bar at $f_0 = 23.0$ kHz. The initial conditions for the ODE system are: $R_i = R_0$, $\dot{R}_0 = 0.0\frac{\text{m}}{\text{s}}$, $T_b^0 = T_l$, $x_0 = 0.10$ mm, $\dot{x}_0 = 0.0\frac{\text{m}}{\text{s}}$, $y_0 = -0.15$ mm, $\dot{y}_0 = 0.0\frac{\text{m}}{\text{s}}$, $z_0 = 0.10$ mm, $\dot{z}_0 = 0.0\frac{\text{m}}{\text{s}}$. The simulation was made during 10000 radial cycles. For these particular parameters the bubble translates to a mean position $x_m = 0.0$ mm, $y_m = 0.0$ mm, $z_m = 0.19$ mm above the pressure antinode without describing pseudo-orbits. This is in agreement with [Toegel et al. \(2006\)](#) calculations which predict shape and path stability for a bubble under these conditions. The black point indicates the origin of coordinates.